

LIMITS ON ARC-MINUTE-SCALE COSMIC MICROWAVE BACKGROUND ANISOTROPY AT 28.5 GHz

W. L. HOLZAPFEL,¹ J. E. CARLSTROM,² L. GREGO,³ G. HOLDER,² M. JOY,⁴ AND E. D. REESE²

Received 1999 November 21; accepted 2000 March 24

ABSTRACT

We have used the Berkeley-Illinois-Maryland Association (BIMA) millimeter array outfitted with sensitive centimeter-wave receivers to search for cosmic microwave background (CMB) anisotropies on arc-minute scales. The interferometer was placed in a compact configuration that produces high brightness sensitivity, while providing discrimination against point sources. Operating at a frequency of 28.5 GHz, the FWHM primary beam of the instrument is ~ 6.6 . We have made sensitive images of seven fields, four of which were chosen specifically to have low IR dust contrast and to be free of bright radio sources. Additional observations with the Owens Valley Radio Observatory (OVRO) millimeter array were used to assist in the location and removal of radio point sources. Applying a Bayesian analysis to the raw visibility data, we place limits on CMB anisotropy flat-band power of $Q_{\text{flat}} = 5.6_{-5.6}^{+3.0} \mu\text{K}$ and $Q_{\text{flat}} < 14.1 \mu\text{K}$ at 68% and 95% confidence, respectively. The sensitivity of this experiment to flat-band power peaks at a multipole of $l = 5470$, which corresponds to an angular scale of $\sim 2'$. The most likely value of Q_{flat} is similar to the level of the expected secondary anisotropies.

Subject headings: cosmic microwave background — cosmology: observations

1. INTRODUCTION

The cosmic microwave background (CMB) has the potential to be a powerful probe of the early universe. In the standard inflationary model, the CMB is imprinted with anisotropies that reflect the distribution of matter at the epoch of recombination. Observations of the CMB at degree angular scales probe structures that have recently collapsed at this epoch and for which the distribution of anisotropies is extremely sensitive to the cosmological model. On scales smaller than a few arcminutes, photon diffusion and the finite time of recombination damp the primordial fluctuations to near zero amplitude (Hu & White 1997). However, the subsequent reionization of the universe can create a host of secondary anisotropies of the CMB. For a review of the subject, see Haiman & Knox (1999). On arcminute scales, secondary anisotropies generated since recombination are likely to dominate the primary signal.

There have been many previous searches for anisotropy in the CMB on arcminute scales; both interferometric and single-dish techniques have been used successfully. This paper describes a search for arcminute-scale CMB anisotropies with the Berkeley-Illinois-Maryland Association (BIMA) interferometer in a compact configuration at 28.5 GHz. We begin with a discussion of the instrument, field selection, and observations in § 2. Section 3 describes initial data reduction, including point-source detection and measurement. The Bayesian maximum-likelihood analysis we apply to the data is described in § 4. The results of applying this formalism to our data are presented in § 5, including a discussion of the effects of point-source subtraction. Section 6 discusses the levels of the expected signals. We summarize the previous work in this field in § 7. Finally, in § 8, we

summarize the results and discuss prospects for future observations.

2. INSTRUMENT & OBSERVATIONS

The advent of low-noise, broadband, millimeter-wave amplifiers has made interferometry a particularly attractive technique for detecting and imaging low-contrast emission, such as anisotropy in the CMB. An interferometer directly samples the Fourier transform of the intensity distribution on the sky. By transforming the interferometer output, images of the sky are obtained that include angular scales determined by the size and spacing of the individual array elements. This section describes the BIMA instrument, the selection of the fields, and their observation.

2.1. Instrument

The anisotropy observations described here were made with nine elements of the BIMA array outfitted with sensitive centimeter-wavelength receivers. The BIMA antennas are 6.1 m in diameter and produce 6.6 beams at 28.5 GHz. The receivers are based on low-noise high electron mobility transistor (HEMT) amplifiers (Pospieszalski et al. 1995) and are configured to respond only to right-circularly polarized radiation. At the operating frequency of 28.5 GHz, the receiver noise temperatures range from 13 to 18 K, and the system temperatures were typically 35–55 K, depending on source elevation. The signals from the individual array elements are combined in the BIMA 2 bit digital correlator, which was configured for these observations with eight contiguous 100 MHz sections of 32 channels each. The array elements were placed in a compact two-dimensional configuration, which provides high brightness sensitivity as well as sufficient resolution to identify radio point sources.

We have also made supporting observations with the Owens Valley Radio Observatory (OVRO) array outfitted with the same centimeter-wave receivers. These observations were used primarily for locating and measuring point sources in the observed fields. The OVRO antennas are 10.4 m in diameter and produce 3.8 beams at 28.5 GHz. For a description of the instrument, see Carlstrom, Joy, & Grego (1996). The BIMA and OVRO arrays, outfitted with

¹ Department of Physics, University of California, Berkeley, CA 94720.

² Department of Astronomy and Astrophysics, University of Chicago, Chicago, IL 60637.

³ Harvard-Smithsonian Center for Astrophysics, Mail Stop 83, 60 Garden Street, Cambridge, MA 02138.

⁴ Space Science Laboratory, SD50, NASA Marshall Space Flight Center, Huntsville, AL 35812; swlh@cfpa.berkeley.edu.

TABLE 1
FIELD POSITIONS AND OBSERVATION TIMES

Field	α (J2000)	δ (J2000)	Observation Year(s)	Time (hr)
BDF1.....	16 45 11.3	+46 24 56	1997, 1998	43.1
BDF2.....	13 12 17.4	+42 38 05	1997	35.5
BDF3.....	00 30 16.4	+17 02 40	1997	36.6
BDF4.....	00 28 04.4	+28 23 06	1998	77.6
BDF5.....	12 36 49.4	+62 12 58	1998	32.0
BDF6.....	18 21 00.0	+59 15 00	1998	43.5
BDF7.....	06 58 45.0	+55 17 00	1998	44.7

NOTE.—Units of right ascension are hours, minutes, and seconds, and units of declination are degrees, arcminutes, and arcseconds.

centimeter-wavelength receivers, have been used to image more than 20 clusters (Carlstrom et al. 1999).

2.2. Field Selection

This paper reports the results of a search for CMB anisotropy in seven independent fields. Two of the fields, BDF1 and BDF2, are centered at the positions of two claimed microwave decrements discovered in deep integrations with the Ryle and VLA interferometers (Jones et al. 1997; Richards et al. 1997). A companion paper (Holzapfel et al. 2000) demonstrates that our data are inconsistent with models used to describe the claimed decrements and show no evidence for the existence of the claimed decrements. In 1997, we observed a third field, BDF3, in the direction of the radio-quiet quasar PSS 0030+1702, which was originally selected as a distant cluster candidate. The quasar is at redshift $z = 4.28$ and has two Ly α -break galaxies within 10" (G. Djorgovski 1997, private communication). The way in which these three fields were selected would prevent us from claiming that they could produce an unbiased measurement of CMB anisotropy. However, for the purpose of placing upper limits on CMB anisotropy, we are justified in making use of these observations.

In 1998, four additional fields were selected so as to be evenly distributed in right ascension and at convenient declinations for observations with the BIMA array. The fields were chosen to be in regions of low dust emission and contrast, as determined from examination of *IRAS* 100 μ m maps. One of these fields, BDF4, was chosen to overlap the Hubble Deep Field. The VLA NVSS (Condon et al. 1998) and FIRST (White et al. 1997) surveys were then used to select regions free of bright point sources at 1.4 GHz. Finally, we used the SkyView⁵ Digitized Sky Survey and *ROSAT* All-Sky Survey maps to check for bright optical or X-ray emission, which could complicate follow-up observations. The pointing centers for each of the seven fields are given in Table 1.

For one of the new fields, we used the OVRO array to check for radio sources at 28.5 GHz before beginning observations with the BIMA array. With a seven-pointing mosaic, we reached a map rms flux density of $\sim 120 \mu$ Jy over a 8' region containing the entire BDF4 field observed with BIMA. We discovered a single source with a flux density of 1.4 mJy. This and all flux densities in this paper have been corrected for the attenuation of the primary beam, unless otherwise specified. The pointing center for the

BIMA observations was chosen so that this source lay outside the observed field of view. Unfortunately, we did not have time to image all the observed fields with the OVRO array, and it is possible that some of the fields observed in 1998 suffer from low-level point-source contamination.

2.3. BIMA Observations

All observations were made during the summers of 1997 and 1998, interspersed between observations of the Sunyaev-Zeldovich effect (SZE) in X-ray-selected clusters. In 1998, we selected four fields spaced in right ascension so that at any given time, one of them had an hour angle suitable for observation. Each 20 minute source observation was bracketed by the observation of a calibration source. Including the time for calibration cycles, the fraction of time spent on-source was $\sim 60\%$. The integration times for each of the seven fields are given in Table 1. The flux densities of the calibration sources are all referenced to the flux density of Mars, which is uncertain by approximately 4% (see discussion in Grego 1998).

3. EDITING AND INSPECTION

The data are edited using several criteria to ensure the integrity of the calibration and that the results remain free of systematics. It is possible for the beam of one dish to be obscured by one of its neighbors in the array. Baselines involving telescopes within 3% of the shadowing limit are discarded. The spectral channels are inspected for any interference and removed if they are believed to be contaminated. Low signal-to-noise ratio channels near the edges of the correlated bandwidth are not used. The effective noise bandwidth of the correlator after accounting for the 2 bit digitization and removed end channels is ~ 540 MHz. Records with spurious system temperatures, caused by failed or aborted calibration cycles, are discarded. Source data not bracketed by successful calibration cycles are discarded. During periods of poor weather, the phase coherence of the calibration sources becomes poor. All data that are bracketed by calibration cycles with poor phase coherence are also discarded.

3.1. Point Sources

Each data set is transformed to create a map with the DIFMAP package (Pearson et al. 1994). The maps are then searched for statistically significant unresolved emission. In order to remain unbiased in our search for point sources, we limit ourselves to the range of baselines greater than $2.4 k\lambda$ ($l > 15000$), which are completely independent of the baselines used in the anisotropy analysis. In this way we can be assured that the anisotropy results will not systematically depend on the point-source detection and subtraction. In general, we find the flux density and positions of the sources by fitting the Fourier transform of the source model directly to the visibility data. The source model is multiplied by the measured primary beam response in order to take the attenuation of the source into account. Table 2 lists the positions and flux densities of the significant point sources in the observed fields.

The brightest point source discovered was centered at $\alpha = 00^{\text{h}}30^{\text{m}}37^{\text{s}}.0$, $\delta = +17^{\circ}05'12''$ (J2000), offset from the pointing center of the BDF3 field by $\Delta\alpha = +294''$ and $\Delta\delta = +152''$. The observed flux density is attenuated by the

⁵ We acknowledge the use of NASA's SkyView facility (<http://skyview.gsfc.nasa.gov>), located at NASA Goddard Space Flight Center.

TABLE 2
SUBTRACTED POINT SOURCES

SOURCE	POSITION (J2000)		DISTANCE FROM MAP CENTER		FLUX (μ Jy)
	α	δ	$\Delta\alpha$ (arcsec)	$\Delta\delta$ (arcsec)	
BDF3 J003037.0+170512.....	00 30 37.0	+17 05 12	294	152	12800 \pm 1600
BDF5 J123644.4+621133.....	12 36 44.4	+62 11 33	-34	-85	347 \pm 59
BDF1 J164520.9+462543.....	16 45 20.9	+46 25 43	100	47	227 \pm 63
BDF1 J164512.5+462413.....	16 45 12.5	+46 24 13	6	-43	222 \pm 63
BDF1 J164523.0+462421.....	16 45 23.0	+46 24 21	115	-36	262 \pm 71

NOTE.—Coordinates, distances from the anisotropy map center, and intrinsic flux densities of the significant sources in the observed fields at 28.5 GHz. Units of right ascension are hours, minutes, and seconds, and units of declination are degrees, arcminutes, and arcseconds.

finite size of the array element beams, which are measured to have a FWHM of $\sim 396''$. This source is far from the center of the map and has an observed flux density of 1.5 mJy. Correcting for the primary beam response, the intrinsic source flux density is determined to be 12.8 ± 1.6 mJy.

A significant point source was detected in deep observations of the BDF5 field with both the OVRO and BIMA arrays. There were two pointings of the OVRO array, with one centered on the position of the suspected point source. We simultaneously fitted the raw OVRO and BIMA visibility data with a single-component point-source model. The source is the brightest in the observed field, with a flux density of $347 \pm 59 \mu$ Jy, and was offset from the BDF5 field pointing center by $\Delta\alpha = -34''$ and $\Delta\delta = -85''$. This source has the same position as the brightest source found in a deep radio image made of the HDF with the VLA at 8.4 GHz (Richards et al. 1998).

Observations of the BDF1 field with the Ryle telescope at 15 GHz (Jones et al. 1997) found three significant point sources. In addition to our observations with the BIMA array, we have also imaged this same region with three pointings of the OVRO array operating at 28.5 GHz, each of which were chosen to place the map center near one of the suspected point sources. The entire BDF1 field was imaged with rms flux density ranging from 40 to 100 μ Jy beam $^{-1}$. We have performed a simultaneous fit to the BIMA and OVRO visibility data in order to determine the positions and flux densities of the sources at 28.5 GHz. The flux densities of the sources have been determined using two different methods. First, we fixed the positions of the sources to the positions found with the Ryle observations and solved for the three source flux densities. Introducing these three free parameters decreased the χ^2 of the fit to the visibility data by 25; this indicates that the field suffers significant contamination from these sources. The uncertainties for the source flux densities correspond to the change in flux density that results in an increase in χ^2 of one, while the other free parameters (two other flux densities) are allowed to assume their best-fit values.

We repeated this analysis allowing the source positions as well as flux densities to vary. This procedure allows for differences in the positions determined by the BIMA and OVRO analysis and those of Jones et al. (1997). By allowing the positions to vary, and adding six new free parameters to the model, the χ^2 of the fit is reduced by 14 from the case in which the source positions are fixed to the Ryle positions. Therefore, the differences from the Ryle positions are significant, and in the rest of this work we adopt these new source positions. The differences between each of the new positions

and those of Jones et al. (1997) are less than $6''$. When the uncertainties in the Ryle positions and those found here are taken into account, the positions determined by the two experiments are found to be consistent. The uncertainty for each of the point-source flux densities corresponds to the change in flux density required to produce to a change in the χ^2 of one, while the free parameters (flux density of the other two sources and the positions of all three sources) are allowed to assume their best-fit values. Table 2 lists the measured positions and flux densities of all the detected sources. These sources are removed from the raw data by taking the Fourier transform of the point-source model modulated by the primary beam response and subtracting it directly from the visibility data.

3.2. Image Statistics

We have produced and analyzed images for each of the observed fields. The results for the long-baseline data used in point-source subtraction are listed in Table 3. We limit the data to baselines above 2.4 k λ to guarantee that the data used to determine the point-source flux densities and positions are completely independent of the anisotropy data. The rms for all the data is considerably lower. The map rms indicates the accuracy with which the flux density of point sources can be measured with this subset of the BIMA data. For the BDF1 and BDF5 fields, the point-source sensitivity is considerably better than listed here, due to the supporting OVRO observations. The results using only the short baselines used in the anisotropy analysis are listed in Table 4. For the short-baseline maps, we also express our results in terms of the rms Rayleigh-Jeans (RJ) temperature fluctuations. For both the short- and long-baseline maps, the observed rms values are compared to those expected from

TABLE 3
IMAGE ANALYSIS FOR BASELINES GREATER THAN 2.4 k λ

FIELD	BEAM SIZE (arcsec)	MAP rms (μ Jy beam $^{-1}$)	
		Estimated	Measured
BDF1.....	18.9 \times 25.0	132	139
BDF2.....	18.8 \times 26.0	134	122
BDF3.....	18.1 \times 25.2	155	150
BDF4.....	21.2 \times 21.6	136	127
BDF5.....	22.5 \times 23.9	195	207
BDF6.....	21.7 \times 23.6	152	160
BDF7.....	21.6 \times 23.2	158	157

NOTE.—Image statistics for maps created using only the long baselines used to measure point sources.

TABLE 4
IMAGE ANALYSIS FOR u - v RANGE 0.63–1.2 $k\lambda$

FIELD	BEAM SIZE ($''$)	rms ($\mu\text{Jy beam}^{-1}$)		rms ^a (μK)	
		Estimated	Measured	Estimated	Measured
BDF1.....	98.3 × 116.1	187	191	24.6	25.1
BDF2.....	95.2 × 113.4	225	223	31.3	31.0
BDF3.....	99.1 × 115.5	202	203	26.5	26.6
BDF4.....	108.9 × 118.8	127	99	14.7	11.5
BDF5.....	110.9 × 122.0	206	168	22.8	18.6
BDF6.....	108.4 × 122.4	174	224	19.7	22.4
BDF7.....	105.2 × 148.0	252	304	24.3	29.3

NOTE.—Image statistics for maps created using only the short baselines used in the anisotropy analysis.

^a Image results in rms RJ map temperature.

the noise properties of the visibilities. For the short-baseline results, there are approximately 10 independent beams in each observed field. If we assume that the map values are dominated by Gaussian-distributed noise, the measured rms should be the same as the estimated value within approximately 10% at 68% confidence.

4. ANALYSIS

Several recent papers have dealt with the analysis of CMB data from interferometers (Martin & Partridge 1988; Subrahmanyan et al. 1993; Hobson, Lasenby, & Jones 1995; Hobson & Magueijo 1996; Partridge et al. 1997; White et al. 1999). In this work, we follow the formalism presented in White et al. (1998) for the Bayesian analysis of CMB data.

In theories that predict Gaussian temperature fluctuations, the fundamental theoretical construct is the correlation matrix of the measured data. Since the data are the visibilities measured at a set of points \mathbf{u}_i , we will need to know the correlation matrices for the signal and noise of the observed visibilities. The measured flux densities are given by

$$V(\mathbf{u}) = \frac{\partial B_v}{\partial T} \int d\mathbf{x} \Delta T(\mathbf{x}) A(\mathbf{x}) e^{2\pi i \mathbf{u} \cdot \mathbf{x}}, \quad (1)$$

where $\Delta T(\mathbf{x})$ is the temperature distribution on the sky, $A(\mathbf{x})$ is the primary beam of the telescope,

$$\frac{\partial B_v}{\partial T} = 2k_B \left(\frac{k_B T}{hc} \right)^2 \frac{x^4 e^x}{(e^x - 1)^2}, \quad (2)$$

k_B is Boltzmann's constant, and $x \equiv hv/k_B T_{\text{CMB}}$. We define the visibility correlation matrix,

$$\begin{aligned} C_{ij}^V &\equiv \langle V^*(\mathbf{u}_i) V(\mathbf{u}_j) \rangle \\ &= \left(\frac{\partial B_v}{\partial T} \right)^2 \int_0^\infty w dw S(w) W_{ij}(w), \end{aligned} \quad (3)$$

which is proportional to the product of the power spectrum, $S(w)$, and the visibility window function. The window function is given by

$$W_{ij}(|\mathbf{w}|) \equiv \int_0^{2\pi} d\theta_w \tilde{A}^*(\mathbf{u}_i - \mathbf{w}) \tilde{A}(\mathbf{u}_j - \mathbf{w}), \quad (4)$$

where $\tilde{A}(\mathbf{u})$ is the Fourier transform of the telescope primary beam. In the case of a single flat-band power and $l > 60$, we

can write

$$C_{ij}^V = \frac{6}{5\pi} \left(\frac{\partial B_v}{\partial T} \right)^2 Q_{\text{flat}}^2 \int_0^\infty \frac{dw}{w} W_{ij}(w), \quad (5)$$

where

$$Q_{\text{flat}}^2 \equiv \frac{5}{24\pi} C_l l(l+1) \quad (6)$$

is the normalization of the power spectrum. The correlation function of the noise is diagonal, with elements given by

$$C_{ii}^N = \frac{1}{\sigma_i^2}, \quad (7)$$

where σ_i is the variance of the measured visibilities. For a given set of n measured visibilities, one can test any theory, or set of $\{C_{ij}\}$, by constructing the likelihood function (for complex visibilities)

$$\mathcal{L}(\{C_{ij}\}) = \frac{1}{\pi^n \det C} \exp[-V^*(\mathbf{u}_i) C_{ij}^{-1} V(\mathbf{u}_j)], \quad (8)$$

where $C_{ij} = C_{ij}^V + C_{ij}^N$ is the correlation matrix of visibilities at \mathbf{u}_i and \mathbf{u}_j (Hobson et al. 1995).

4.1. Joint Confidence Intervals

Invoking Bayes' theorem and assuming a uniform prior for the amplitude of the fluctuations, we can determine the probability that the correct result is contained in an interval I ,

$$P(I) = \frac{\int_I \mathcal{L}(z) dz}{\int_0^\infty \mathcal{L}(z) dz}. \quad (9)$$

The confidence interval corresponding to a probability P_0 is given by the I_0 such that $P(I_0) = P_0$ and $\mathcal{L}[z \in I_0] \geq \mathcal{L}[z \notin I_0]$. If the fields are entirely independent, the joint likelihood for the combination of the data sets to be described by a given model is simply equal to the product of the likelihoods for the individual data sets,

$$\mathcal{L}(z) = \prod_i \mathcal{L}_i(z). \quad (10)$$

Combining the diagonal window functions corresponding to each visibility weighted by the noise, we can construct an effective diagonal window function to determine where the

experiment is most sensitive;

$$\bar{W}_l = \sum_i \frac{W_{ii}(l)w_i}{\sum_i \{[W_{ii}(l)/l]\} \sum_i w_i}, \quad (11)$$

where $w_i = 1/\sigma_i^2$. With this normalization,

$$\sum_l \frac{\bar{W}_l}{l} = 1. \quad (12)$$

Using the data-weighted window function, we can determine the effective multipole of the experiment, assuming the power spectrum is flat:

$$l_{\text{eff}} = \sum_l \bar{W}_l. \quad (13)$$

4.2. Binning

The data sets for each of our fields contain on the order of $N = 10^5$ visibilities. The inversion of the covariance matrix required for the analysis is a $N^{2.8}$ process (Press et al. 1996). As discussed in Hobson et al. (1995), considerable compression of the data is necessary if the analysis is to be completed in a reasonable amount of computing time. We divide the u - v plane into a grid of cells; all the visibilities within a cell are combined, weighted by the reciprocal of their estimated noise variance,

$$V_\alpha = \frac{\sum_{i \in \alpha} (V_i/\sigma_i^2)}{\sum_{i \in \alpha} (1/\sigma_i^2)}. \quad (14)$$

We determine noise-weighted u - v positions just as we have determined the values for the visibilities,

$$u_\alpha, v_\alpha = \frac{\sum_{i \in \alpha} (u_i/\sigma_i^2)}{\sum_{i \in \alpha} (1/\sigma_i^2)}, \frac{\sum_{i \in \alpha} (v_i/\sigma_i^2)}{\sum_{i \in \alpha} (1/\sigma_i^2)}. \quad (15)$$

The sampling theorem tells us that the Fourier transform of the sky is completely specified by a sampling of the u - v plane on a regular grid with $\Delta u, \Delta v < 1/2\theta_p$, where θ_p is the angular radius of the primary beam. Because our final u - v points do not form a regular grid, it is possible that we would have to decrease the size of our grid by a factor of 2 to strictly satisfy this criterion. Following Hobson et al. (1995), we define the extent of the beam as the point at which the beam falls to 1% of its peak value, $\theta_p = 7.45$. We determine that the u - v plane must be sampled more densely than $\Delta u, \Delta v = 230$. In practice, this is simple to achieve, and we sample the u - v plane at intervals of $\Delta u, \Delta v = 60$ in the analysis presented in this paper. This compresses the number of u - v points to ~ 200 for each of the data sets.

4.3. Calibration

The likelihood-analysis code has been checked by the analysis of simulated data sets. We took a data file from one of our observations, removed the visibilities, and replaced them with Gaussian-distributed noise with the same weights as the original data. To the noise we added the Fourier transform of a realization of CMB anisotropy with flat-band power that had been modulated with the measured BIMA primary beam. We produced 100 such data sets, each with independent CMB and noise realizations. The simulated data were then analyzed in exactly the same way as the real data, treating each data set as an independent (uncorrelated) observation. For an input flat-band

power with $Q_{\text{flat}} = 30 \mu\text{K}$, we found that the likelihood peaked at $Q_{\text{flat}} = 31 \mu\text{K}$, with values of 29–33 μK and 27–35 μK allowed at 68% and 95% confidence levels, respectively. We interpret this as a demonstration that the analysis code is correctly calibrated.

5. RESULTS

In this section, we use the method described above to determine the relative likelihoods that the observed fields are described by a model for the CMB fluctuations with flat-band power Q_{flat} .

Before proceeding, we discuss the effect on the anisotropy results of subtracting the known point sources. Three of the observed fields are known to have significant point-source contamination. Section 3.1 discusses the determination of the source flux densities and positions. For the three contaminated fields, we subtract the Fourier transform of the point-source model from the raw visibility data. Figure 1 shows the results of the likelihood analysis for the field BDF1 before and after the subtraction of the three detected point sources. The results are normalized to unity likelihood for the case of no anisotropy signal. We have performed the same analysis with the point-source flux densities found when the positions of the sources are fixed to the results of Jones et al. (1997). The results are essentially identical; the most likely value for Q_{flat} is again zero. In all further analysis, we use the point-source flux densities and positions found from the fits to the OVRO and BIMA data. Table 5 lists the results for Q_{flat} from the analysis of the three contaminated fields before point-source subtraction. It is clear that neglecting to subtract the known point sources can lead to an erroneous detection of anisotropy.

Figures 2 and 3 show the relative likelihood for each of the observed fields, after subtracting the detected point sources listed in Table 2. Table 6 lists the 68% and 95% confidence intervals in Q_{flat} for each of the observed fields. The fields are independent, and we can apply equation (10) to determine the joint likelihood for the combination of fields. The relative likelihoods of the joint fits are plotted in Figure 4. Table 6 lists the confidence intervals in Q_{flat} found from the joint fits. Because of the different array configurations and declinations of the sources, the window function

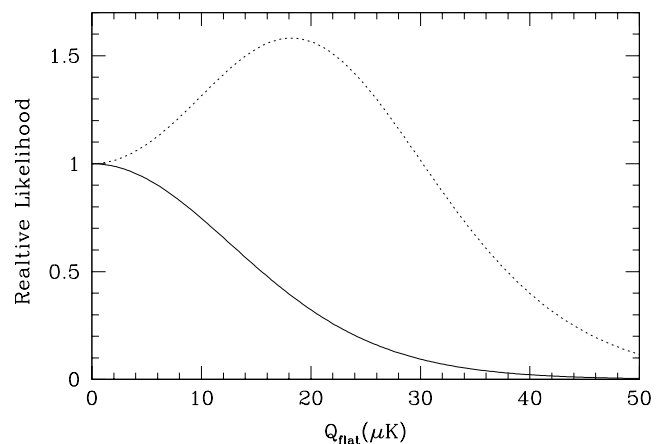


FIG. 1.—Relative likelihood that the observed signal in the BDF1 field is described by flat-band power with amplitude Q_{flat} . The dotted line corresponds to an analysis ignoring the measured point sources, and the solid line shows the result when the measured point-source flux densities are subtracted from the visibility data.

TABLE 5
RESULTS BEFORE POINT-SOURCE SUBTRACTION

FIELD	$Q_{\text{flat}} (\mu\text{K})$		
	Most Likely	68%	95%
BDF1.....	18.2	4.8–29.0	0.0–42.2
BDF3.....	11.8	0.0–31.6	0.0–61.8
BDF5.....	4.8	0.0–17.8	0.0–33.2

NOTE.— Q_{flat} results before subtraction of known point sources. Compare with Table 6 to see the results after point-source removal.

for each observation is slightly different. We have used equation (11) to determine effective diagonal window functions corresponding to the 1997, 1998, and the combination of the 1997 and 1998 data. These window functions are plotted as a function of multipole in Figure 5. Finally, we have used equation (13) to determine the effective multipole number, $l_{\text{eff}} \sim 5470$, of the combination of all the data.

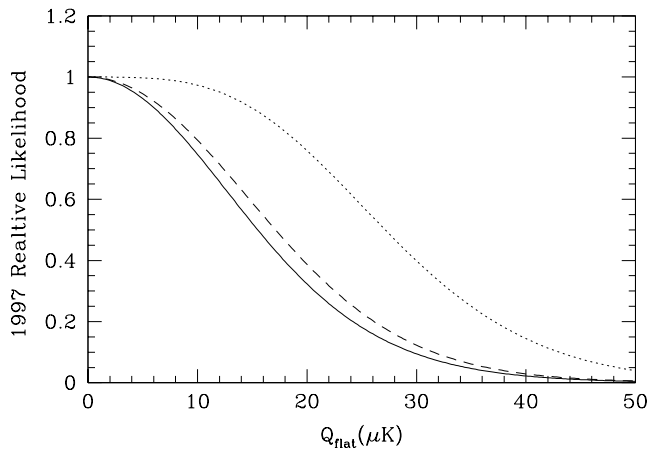


FIG. 2.—Relative likelihood that the observed signal in each of the 1997 data sets is described by a flat-band power with amplitude Q_{flat} . The solid, dotted, and dashed lines show the fields BDF1, BDF2, and BDF3, respectively.

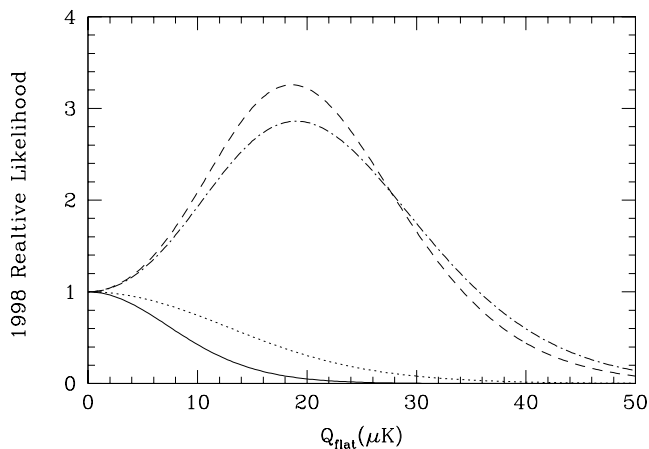


FIG. 3.—Relative likelihood that the observed signal in each of the 1998 data sets is described by flat-band power with amplitude Q_{flat} . The solid, dotted, dashed, and dot-dashed lines show the BDF4, BDF5, BDF6, and BDF7 data, respectively. The fields BDF6 and BDF7 have no supplementary observations with the OVRO array, and subsequently have poor limits on point-source contamination.

TABLE 6
MOST LIKELY Q_{flat} AND CONFIDENCE INTERVALS

FIELD	$Q_{\text{flat}} (\mu\text{K})$		
	Most Likely	68%	95%
BDF1	0.0	0.0–13.1	0.0–26.6
BDF2	0.0	0.0–20.5	0.0–38.0
BDF3	0.0	0.0–14.4	0.0–29.2
Combined 1997 fields.....	0.0	0.0–8.9	0.0–17.4
BDF4	0.0	0.0–8.5	0.0–17.5
BDF5	0.0	0.0–13.0	0.0–26.6
BDF6	18.6	8.8–28.8	0.0–37.8
BDF7	19.0	8.4–30.4	0.0–40.6
Combined 1998 fields.....	8.8	2.4–12.8	0.0–17.4
All fields	5.6	0.0–9.6	0.0–14.1

NOTE.—Results of the Bayesian analysis for each of the observed fields. Col. (2) gives the most likely value for band power amplitude, Q_{flat} . Cols. (3) and (4) give the 68% and 95% confidence intervals, respectively.

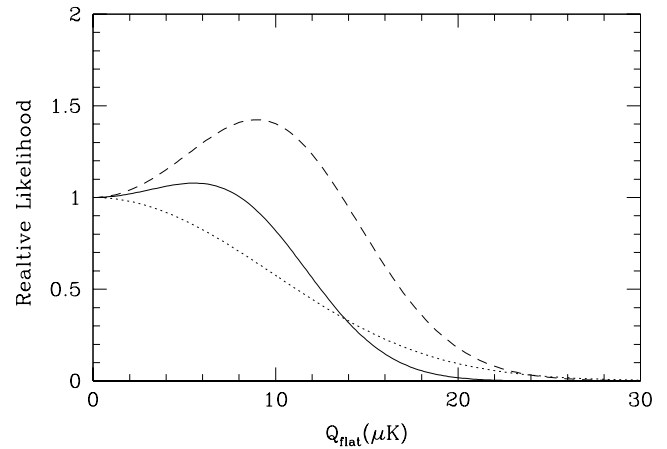


FIG. 4.—Relative joint likelihood that the data from each year is described by flat-band power with amplitude Q_{flat} . The dotted, dashed, and solid lines correspond to the 1997, 1998, and a combination of 1997 and 1998 data, respectively.

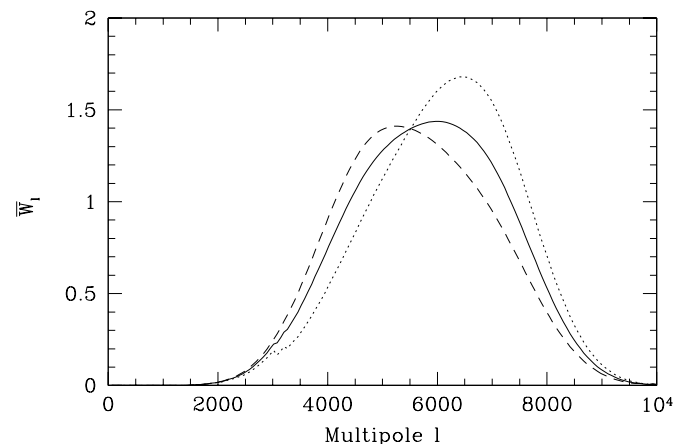


FIG. 5.—“Data-weighted” window functions, \bar{W}_l . The dotted, dashed, and solid lines correspond to the 1997, 1998, and a combination of 1997 and 1998 data, respectively.

One is immediately struck by the fact that the joint likelihood for all the data, shown in Figure 4, peaks at $Q_{\text{flat}} > 0$. However, this result has fairly low significance. Each of the individual fields is consistent with no signal on the sky at 95% confidence, and the confidence of a nonzero Q_{flat} for the joint likelihood is only 44%.

After point-source subtraction, none of the fields observed in 1997 produce a nonzero anisotropy signal. This is further evidence that the BDF1 and BDF2 data are inconsistent with the presence of massive galaxy clusters in these fields, as has been demonstrated by Holzapfel et al. (2000). There is also no evidence for a distant cluster in the BDF3 field. From Table 6, we can see that including the 1997 data in the joint likelihood only reduces the limits on Q_{flat} .

5.1. Limits on Point-Source Contamination

All of the excess power is found in the two fields that have the poorest limits on point-source contamination of any of the seven fields. It is possible that point-source contamination contributes to the signal in these fields. If the observed power is dominated by Poisson-distributed point sources, we expect to find $Q_{\text{flat}} \propto l$. We have verified this scaling by an analysis of both real and simulated data with significant point-source emission. If this scaling was observed in these data sets, it would be a “smoking gun” for point-source contamination.

Two of the fields we have observed, BDF6 and BDF7, yield significant detections of power on short baselines. The flat-band power in these fields, determined from a joint analysis of the 0.63–1.2 k λ data, is found to be $Q_{\text{flat}} = 18.9 \pm 7.2 \mu\text{K}$ at 68% confidence. To determine if this signal is due to point-source contamination, we have reanalyzed the data assuming $Q = Q_0(l/l_0)$ rather than flat-band power. The effective multipole l_0 to which Q_0 is referred is chosen so that $Q_0 = Q_{\text{flat}}$ when both analyses are applied to the 0.63–1.2 k λ data. We have determined Q_0 for several fields with known point sources and find that, for the long baselines (1.2–6.0 k λ), the value of Q_0 is identical to that found from the short baselines (0.63–1.2 k λ) used in the anisotropy analysis. Applying this analysis to the combined long-baseline data for the fields BDF6 and BDF7, we find no evidence for point-source emission and constrain $Q_0 < 8.8 \mu\text{K}$ and $Q_0 < 15.8 \mu\text{K}$ at 68% and 95% confidence, respectively. Therefore, we conclude with 95% confidence that Poisson-distributed point sources cannot be responsible for excess power found in the analysis of the short-baseline data. However, if the signal is produced by several weak clustered point sources, such as in the BDF1 field, the scaling $Q_{\text{flat}} \propto l$ is not observed in either the real or the simulated data. Therefore, weak clustered sources could be responsible for the observed signals.

6. EXPECTED SIGNALS

To interpret our results, it is informative to consider the level of the expected signals. This section gives our best estimates of the expected contributions from primary and secondary CMB anisotropies and foreground sources to the observed Q_{flat} . These results are compiled in Table 7.

6.1. Primary Anisotropies

We have convolved model CMB anisotropy power spectra with the window function of the experiment to

TABLE 7
EXPECTED CONTRIBUTIONS TO Q_{flat}

Signal	Q_{flat} (μK)
Primary Anisotropy	1.1–5.8
Vishniac Effect	1.7–3.6
Inhomogeneous Reionization	1.8–2.5
Sunyaev-Zeldovich Effect	1.3–8.0
Point Sources	< 6.6
Spinning Dust/Free-Free	< 1.1
Total	3.0–12.7

NOTE.—Expected flat-band power due to primary anisotropy, secondary anisotropy, and foreground confusion.

determine the inferred flat-band power signal,

$$Q_{\text{flat}}^2 = \left(\frac{5}{24\pi} \right) \sum_l C_l l \bar{W}_l dl. \quad (16)$$

The CMB power spectra were generated using the CMBFAST code (Seljak & Zaldarriaga 1996). The expected signal for this experiment is largely determined by the total energy density of the universe, Ω_0 . We have calculated Q_{flat} for a range of values for Ω_0 , while keeping the baryon density, $\Omega_B = 0.05$, and the Hubble constant, $h = 0.65$, constant. For these observations, the majority of the signal comes from the small region of overlap between the BIMA array diagonal window function and the damping tail of the CMB. For total energy density $\Omega_0 = 1.0$ and 0.3, we expect primary anisotropy signals of $Q_{\text{flat}} = 1.1$ and $5.8 \mu\text{K}$, respectively.

6.2. Secondary Anisotropies

Some time after recombination at redshift $z \sim 1100$, the universe was reionized. We know that this ionization was essentially complete by redshift $z \sim 5$ because spectra of distant quasars do not show a continuum of absorption by neutral hydrogen (Gunn & Peterson 1965). The interaction of the CMB with the reionized universe leads to secondary anisotropies. There are three types of secondary anisotropies that are expected to make significant contributions on arcminute scales: the Vishniac effect, inhomogeneous reionization, and the SZ effect.

The Vishniac effect is a “second-order” Doppler shift that produces CMB temperature anisotropy by the fact that the large-scale velocity field is modulated by small-scale variations in baryon density (Vishniac 1987; Ostriker & Vishniac 1986). While the other secondary anisotropies discussed in this section require variations in ionization, the Vishniac effect acts in a universe that is uniformly ionized. Hu & White (1996) have determined the size of the effect for a range of reionization histories in the context of a critical CDM model. For reionization epochs $z_r = 5$ and 100, they find signals of amplitude $Q_{\text{flat}} \sim 1.7$ and $3.6 \mu\text{K}$, which peak at multipole moments $l \sim 5000$ and 10,000, respectively.

Inhomogeneous reionization will imprint Doppler shifts, due to the velocities of the reionized regions, on the Compton-scattered CMB photons (Kaiser 1984). The effect of inhomogeneous reionization has been studied most recently by Gruzinov & Hu (1998) and Knox, Scoccimarro, & Dodelson (1998). There are considerable uncertainties in the details of the generation of ionized regions. To obtain an accurate result, the correlation of the ionizing regions must

be taken into account. For universes that reionize at $z_r = 26$ and 31, Knox et al. (1998) find a flat-band temperature anisotropy of $Q_{\text{flat}} \sim 1.8$ and $2.5 \mu\text{K}$ at $l = 5500$. Observation of this signal would provide useful constraints on what are presently highly speculative reionization scenarios.

The majority of luminous matter in massive clusters of galaxies is observed to exist in the form of ionized gas that has been heated by gravitational infall. This hot gas can present a considerable inverse Compton scattering cross section to CMB photons. The resulting spectral distortion in the direction of a cluster of galaxies is known as the Sunyaev-Zeldovich effect (SZE; Sunyaev & Zeldovich 1972). The change in RJ CMB temperature in the direction of a massive cluster can be as large as 1 mK. For a recent review, see Birkinshaw (1999) and references therein. Several authors have computed the expected CMB anisotropy power spectrum due to the SZE in clusters of galaxies (Atrio-Barandela & Mücke 1999; Komatsu & Kitayama 1999; Holder & Carlstrom 1999). The treatments differ in the range of cosmological models considered and the models for the cluster evolution. One general conclusion is that, at the small angular scales relevant for this experiment, the majority of the signal is due to distant, less massive clusters, and removing either the bright SZE or X-ray sources does not appreciably change the results. In general, the results depend sensitively on the assumed cosmology and cluster evolution model. For example, Holder & Carlstrom (1999) find that at $l \sim 5000$, $Q_{\text{flat}} = 1.3\text{--}8.0 \mu\text{K}$ for the range of models they consider.

6.3. Undetected Radio Point Sources

Section 3.1 describes our technique for measuring and removing point sources. As seen in Tables 3 and 4, the sensitivity of the data with baselines longer than $2.4 \text{ k}\lambda$ is comparable to that of the $0.63\text{--}1.2 \text{ k}\lambda$ data. Although we see no evidence for additional point sources, we cannot reliably constrain the presence of point sources below 3σ in the high-resolution maps, which corresponds to a flux density of $\sim 300\text{--}500 \mu\text{Jy}$.

We have attempted to quantify the expected signals from point sources both analytically and through simulations. The integrated source counts with flux density less than S_{cut} have been measured at 8.4 GHz by Partridge et al. (1997). We take their result and scale it to the BIMA observing frequency of 28.5 GHz by using the average measured radio power-law index ($\alpha = 0.77$) from Cooray et al. (1998). The number density of sources then becomes

$$N(>S_{\text{cut}}) = \frac{20}{\text{arcmin}^2} \left(\frac{\nu}{8.4 \text{ GHz}} \right)^{-\beta\alpha} \left(\frac{S_{\text{cut}}}{\mu\text{Jy}} \right)^{-\beta}, \quad (17)$$

where $\beta = 1.2$. We follow the treatment of Scott & White (1999) and estimate the contribution to the power spectrum to be

$$C_l \sim \frac{\beta}{(dB/dT)^2(2 - \beta)} N(>S_{\text{cut}}) S_{\text{cut}}^2, \quad (18)$$

where S_{cut} is the minimum source flux density that we can remove from our maps. Using equation (16), we can then determine the contribution of point sources to Q_{flat} . For the maximum residual source flux density, $S_{\text{cut}} = 400 \mu\text{Jy}$, we find $Q_{\text{flat}} = 6.6 \mu\text{K}$.

In order to test this approximation, we simulated distributions of point sources on the sky. For each simulated

sky, we generated a sample of point sources with flux densities less than $S_{\text{cut}} = 400 \mu\text{Jy}$ drawn from the dN/dS distribution given by Partridge et al. (1997). The sources are placed at random in the field. These model skies are then Fourier transformed and added to a unique manifestation of visibilities consistent with the weights of one of our complete data sets. The simulations are then analyzed exactly as the real data. When we analyzed 100 manifestations of the sky generated in this way, we found $Q_{\text{flat}} = 4.8_{-2.8}^{+2.0} \mu\text{K}$ at 68% confidence. Thus, the source simulations and analytic approximation predict similar signals, which, interestingly, are of the same order as the most likely signal in the data.

However, as described in § 1, the observed fields were selected to be free of bright radio sources at 1.4 GHz. If the sources have a falling spectrum, we will have selected fields with significantly lower than typical point-source confusion at 28.5 GHz. Furthermore, for the BDF1 and BDF5 fields, additional OVRO observations were used to remove point sources down to $\sim 200 \mu\text{Jy}$. Therefore, the estimates for point-source contamination presented here are upper limits to the expected signal in our data.

6.4. Anomalous Dust Emission

Recently, anomalous foreground emission at microwave frequencies has been observed that is found to be strongly correlated with *IRAS* 100 μm maps (Leitch et al. 1997; de Oliveira-Costa et al. 1997). It has been proposed that this emission may be due to either free-free emission (Kogut et al. 1996) or dipole emission from rapidly spinning dust grains (Draine & Lazarian 1997). From a compilation of experimental results, Kogut (1999) has determined a scaling between intensity in the *IRAS* 100 μm band and the brightness temperature at microwave frequencies. At 28.5 GHz, we expect this scaling to be approximately $17 \mu\text{K}/(\text{MJy sr}^{-1})$. As mentioned in § 2.2, we selected fields to have minimal 100 μm emission and contrast. We have determined the rms 100 μm intensity for each of our observed fields. The resolution of the *IRAS* maps is 1'.5, well matched to the angular scale on which the BIMA experiment is sensitive. The observed fields are found to have a range of rms fluctuations, $\Delta I_{100 \mu\text{m}} = 0.04\text{--}0.09 \text{ MJy sr}^{-1}$. Therefore, we expect an rms temperature signal from this foreground of $\Delta T < 1.7 \mu\text{K}$, which corresponds to $Q_{\text{flat}} < 1.1 \mu\text{K}$.

6.5. Systematic Errors

The detected anisotropy could also be the result of subtle systematic errors. The observations presented here represent the deepest images we have made of fields without strong SZE decrements due to known galaxy clusters, and therefore could be subject to undiscovered systematic errors. Without success, we have extensively searched for a nonastronomical explanation of the observed excess power. The results are found to be constant across the observing frequency band, independent of baseline or telescope, reproducible from day to day, and uncorrelated with the position of the sun or moon during our observations. If this work is subject to systematic errors, deeper observations will be necessary in order for them to manifest themselves in a significant manner.

7. COMPARISON WITH PREVIOUS WORK

There here have been many previous searches for anisotropy in the CMB at arcminute scales. The results of this

earlier work have been expressed in several different ways. Until recently, it was common for experimenters to quote limits on CMB anisotropies with a Gaussian autocorrelation function (GACF),

$$C(\theta) = C_0 \exp\left(-\frac{\theta^2}{2\theta_c^2}\right), \quad (19)$$

where θ_c is the coherence angle and $C_0^{1/2}$ is the variance of the CMB. Given the diagonal elements of the average window function, it is simple to convert between flat-band power and GACF results (Bond 1995). Here we express our results in terms of limits on temperature anisotropy with a GACF in order to facilitate comparison with the results of other experiments. At the scale of maximum sensitivity, $\theta_c = 0.9$, our 68% and 95% confidence limits on $C_0^{1/2}/T_{\text{CMB}}$ are 6.5×10^{-6} and 9.6×10^{-6} , respectively.

In previous work, both single-dish and interferometric techniques have been used to perform sensitive searches for CMB anisotropies on arcminute scales. Table 8 lists the frequency, sky coverage, coherence angle corresponding to maximum sensitivity, and 95% confidence limits on variance and flat-band power for each of the most sensitive experiments and compare them with our results.

Operating at a frequency of 20 GHz, the Owens Valley Radio Observatory (OVRO) 40 m dish has been used to measure sensitive differences between beams of 1.8 FWHM beams separated by 7' (Readhead et al. 1989). They express their results in terms of limits on fluctuations with a GACF. At the coherence angle for which the experiment is maximally sensitive, $\theta_c = 2.6$, they constrain $C_0^{1/2}/T_{\text{CMB}} < 1.7 \times 10^{-5}$ at 95% confidence. The effective total sky coverage of the experiment is estimated to be ~ 60 arcmin². More recently, the OVRO Ring experiment used the OVRO 40 m telescope to make a significant detection of anisotropy in a field near the north celestial pole (Myers, Readhead, & Lawrence 1993). These results are inconsistent with the earlier work at OVRO and are likely to suffer from foreground contamination.

The SuZIE experiment is a drift-scanning bolometer array. Fielded at the CalTech Submillimeter Observatory (CSO), it was used to map ~ 213 arcmin² of blank sky at its operating frequency of 142 GHz (Church et al. 1997). Unlike the other experiments discussed here, radio point sources are not a significant source of confusion for SuZIE. They also express their results in terms of limits on fluctuations with a GACF. At the coherence angle of maximum sensitivity, $\theta_c = 1.1$, they find $C_0^{1/2}/T_{\text{CMB}} < 2.1 \times 10^{-5}$ at 95% confidence.

Interferometers have also proved to be very effective for making sensitive maps of the sky with arcminute resolution.

Using the Very Large Array (VLA) at 8.4 GHz, Partridge et al. (1997) obtained an extremely deep 21 arcmin² image of the sky. On the scale at which the experiment is most sensitive (resolution $\sim 60''$), they find $\Delta T/T_{\text{CMB}} < 2.0 \times 10^{-5}$ at 95% confidence, which corresponds to $Q_{\text{flat}} < 35.2$ μK . In order to achieve this limit, they are forced to subtract a statistical estimate of the image variance due to point sources. Because we do not have exact knowledge of the window function of the VLA observations, we cannot determine the response of their system to CMB anisotropy with a GACF.

A group working with the Australian Telescope Compact Array (ATCA) has recently produced what were, previous to this work, the lowest limits on arcminute-scale CMB anisotropies (Subrahmanyan et al. 1998). They observed at a lower frequency of 8.45 GHz, but the larger size of the ATCA dishes compensates to make the window functions of the ATCA and BIMA experiments similar. Using a single deep pointing of their array (~ 28 arcmin²), they constrained $Q_{\text{flat}} < 23.6$ μK at 95% confidence on an angular scale corresponding to $l_{\text{eff}} \sim 4600$. They also express their results in terms of anisotropy with a GACF. At the coherence angle for which the experiment is maximally sensitive, $\theta_c = 1.0$, they find $C_0^{1/2}/T_{\text{CMB}} < 1.6 \times 10^{-5}$ at 95% confidence.

8. CONCLUSION

We have used the BIMA array in a compact configuration at 28.5 GHz to search for CMB anisotropy in seven independent fields. With these observations, we have placed the lowest limits on arcminute-scale CMB anisotropies to date. These results are determined from ~ 240 arcmin² of sky; this is the largest sky coverage of any of the arcminute-scale anisotropy experiments. In the context of an assumed flat-band power model for the CMB power spectrum, we find $Q_{\text{flat}} = 5.6_{-5.6}^{+3.0}$ μK at 68.3% confidence and $Q_{\text{flat}} < 14.1$ μK at 95.4% confidence, with sensitivity centered about the harmonic multipole $l_{\text{eff}} = 5470$. This result includes the three fields observed in 1997, which were previously suspected to contain possible distant clusters. None of these fields contribute to the observed excess power.

A detection of anisotropy is not surprising when one considers the level of the signals expected from secondary CMB anisotropies and foreground emission. We have ruled out Poisson-distributed point sources as the cause of the detected excess power at greater than 95% confidence, although faint clustered sources could still be responsible. It is possible that we have detected secondary CMB anisotropies or clustered faint radio point sources; however, the confidence of the detection is only 44%.

TABLE 8
COMPARISON WITH PREVIOUS WORK

EXPERIMENT	ν (GHz)	Ω_{sky} (arcmin ²)	θ_c (arcmin)	95% Confidence Limits	
				$C_0^{1/2}/T_{\text{CMB}}$	Q_{flat}
SuZIE	142	213	1.1	2.1×10^{-5}	...
OVRO 40 m.....	20	~ 60	2.6	1.7×10^{-5}	...
VLA	8.4	20	~ 1.0	...	35.2
ATCA	8.4	28	1.0	1.6×10^{-5}	23.6
BIMA	28.5	240	0.9	9.6×10^{-6}	14.1

NOTE.—Frequency, sky coverage, coherence angle, and 95% confidence limits on the variance and flat-band power from previous work and the BIMA results.

In the coming year, we plan to expand our observations to include greater sky coverage and deep searches for point sources. Future observations with broader correlated bandwidth could reach sensitivities an order of magnitude higher than presented here. With proper characterization of foregrounds, these observations may be able to place interesting constraints on models for the reionization of the universe.

Many thanks to the staff of the BIMA and OVRO observatories for their contributions to this project. In particular, a high five to Dick Plambeck, Rick Forster, and John Lugten for their help with the BIMA observations. We would also like to thank Cheryl Alexander for her help in

the construction of the centimeter-wave receivers. Thanks to Asantha Cooray and Sandy Patel for help with the OVRO and BIMA observations. Radio Astronomy with the OVRO millimeter array is supported by NSF grant AST 96-13717. The BIMA millimeter array is supported by NSF grant AST 96-13998. J. E. C. acknowledges support from a NSF-YI grant and the David and Lucile Packard Foundation. E. D. R. and L. G. acknowledge support from NASA GSRP fellowships. This work is supported in part by NASA LTSA grant NAG5-7986. Finally, we would like to acknowledge informed discussions with Martin White and Ravi Subrahmanyan.

REFERENCES

- Atrio-Barandela, F., & Mückel, J. P. 1999, *ApJ*, 515, 465
 Birkinshaw, M. 1999, *Phys. Rep.*, 310, 97
 Bond, R. 1995, *Astrophys. Lett. Commun.*, 32, 63
 Carlstrom, J. E., Joy, M., & Grego, L. 1996, *ApJ*, 456, L75
 Carlstrom, J. E., Joy, M., Grego, L., Reese, E. D., Patel, S., Holder, G., Cooray A., & Holzzapfel, W. L. 1999, *Phys. Scr.*, 60, in press (preprint astro-ph/9905255)
 Church, S. E., Ganga, K. M., Holzzapfel, W. L., Ade, P. A. R., Mauskopf, P. D., Wilbanks, T. M., & Lange A. E. 1997, *ApJ*, 484, 523
 Condon, J. J., Cotton, W. D., Greisen, E. W., Yin, Q. F., Perley, R. A., Taylor, G. B., & Broderick, J. J. 1998, *AJ*, 115, 1693
 Cooray, A. R., Grego, L., Holzzapfel, W. L., Joy, M., & Carlstrom, J. E. 1998, *AJ*, 115, 1388
 de Oliveira-Costa, A., Kogut, A., Devlin, M. J., Netterfield, C. B., Page, L. A., & Wollack, E. J. 1997, *ApJ*, 482, L17
 Draine, B. T., & Lazarian, A. 1998, *ApJ*, 494, L19
 Grego, L. 1998, Ph.D. thesis, Caltech
 Gruzinov, A., & Hu, W. 1998, *ApJ*, 508, 435
 Gunn, J. E., & Peterson, B. A. 1965, *ApJ*, 142, 1633
 Haiman, Z., & Knox, L. 1999, in *ASP Conf. Ser. 181, Microwave Foregrounds*, ed. A. de Oliveira-Costa & M. Tegmark (San Francisco: ASP), 227
 Hobson, M. P., Lasenby, A. N., & Jones, M. 1995, *MNRAS*, 275, 863
 Hobson, M. P., & Magueijo, J. 1996, *MNRAS*, 283, 1133
 Holder, G., & Carlstrom, J. E. 1999, in *ASP Conf. Ser. 181, Microwave Foregrounds*, ed. A. de Oliveira-Costa & M. Tegmark (San Francisco: ASP), 199
 Holzzapfel, W. L., Carlstrom, J. E., Joy, M., Grego, L., & Reese, E. D. 2000, *ApJ*, 533, 38
 Hu, W., & White, M. 1996, *A&A*, 315, 33
 ———. 1997, *ApJ*, 479, 568
 Jones, M. E., Saunders, R., Baker, J. C., Cotter, G., Edge, A., Grainge, K., Hayes, T., Lasenby, A., Pooley, G., & Röttgering, H. 1997, *ApJ*, 479, L1
 Kaiser, N. 1984, *ApJ*, 282, 374
 Knox, A., Scoccimarro, R., & Dodelson, S. 1998, *Phys. Rev. Lett.*, 81, 2004
 Kogut, A. 1999, in *ASP Conf. Ser. 181, Microwave Foregrounds*, ed. A. de Oliveira-Costa & M. Tegmark (San Francisco: ASP), 91
 Kogut, A., Banday, A. J., Bennett, C. L., Gorski, K. M., Hinshaw, G., Smoot, G. F., & Wright, E. I. 1996, *ApJ*, 464, L5
 Komatsu, E., & Kitayama, T. 1999, *ApJ*, 526, L1
 Leitch, E. M., Readhead, A. C. S., Pearson, T. J., & Myers, S. T. 1997, *ApJ*, 486, L23
 Martin, H. M., & Partridge, R. B. 1988, *ApJ*, 324, 794
 Myers, S. T., Readhead, A. C. S., & Lawrence, C. R. 1993, *ApJ*, 405, 8
 Ostriker, J. P., & Vishniac, E. T. 1986, *ApJ*, 306, L51
 Partridge, R. B., Richards, E. A., Fomalont, E. B., Kellerman, K. I., & Windhorst, R. A. 1997, *ApJ*, 483, 38
 Pearson, T. J., Shepherd, M. C., Taylor, G. B., & Myers, S. T. 1994, *BAAS*, 26, 48.08
 Pospieszalski, M. W., Lakatos, W. J., Nguyen, L. D., Lui, T., Le, M., Thompson, M. A., & Delaney, M. J. 1995, *Microwave Symp. Digest (IEEE MTT-S Int.)*, 3, 1121
 Press, W. H., Teukolsky, S. A., Vetterling, W. T., & Flannery, B. P. 1996, *Numerical Recipes (2d Ed.)*; Cambridge: Cambridge Univ. Press
 Readhead, A. C. S., Lawrence, C. R., Myers, S. T., Sargent, W. L. W., Hardebeck, H. E., & Moffet, A. T. 1989, *ApJ*, 346, 566
 Richards, E. A., Kellerman, K. I., Fomalont, E. B., Windhorst, R. A., & Partridge, R. B. 1998, *AJ*, 116, 1039
 Richards, E. A., Partridge, R. B., Fomalont, E. B., Kellerman, K. I., & Windhorst, R. A. 1997, *ApJ*, 483, 38
 Scott, D., & White, M. 1999, *A&A*, 346, 1
 Seljak, U., & Zaldarriaga, M. 1996, *ApJ*, 469, 437
 Subrahmanyan, R., Ekers, R. D., Sinclair, M., & Silk, J. 1993, *MNRAS*, 263, 416
 ———. 1998, *MNRAS*, 298, 1189
 Sunyaev, R. A., & Zeldovich, Ya. B. 1972, *Comm. Astrophys. Space Sci.*, 4, 173
 White, M., Carlstrom, J. E., Dragovan, M., & Holzzapfel, W. L. 1999, *ApJ*, 514, 12
 White, R. L., Becker, R. H., Helfand, D. J., & Gregg, M. D. 1997, *ApJ*, 475, 479
 Vishniac, E. T. 1987, *ApJ*, 322, 597